WASHINGTON UNIVERSITY IN ST. LOUIS

The report for Washington University for the period follows.

ENGINEERING DEVELOPMENT OF
SLURRY BUBBLE COLUMN REACTOR (SBCR) TECHNOLOGY

Twenty-third Quarterly Report
for
October 1 - December 31, 2000

(Budget Year 6: October 1, 2000 – September 30, 2001)

Chemical Reaction Engineering Laboratory
Chemical Engineering Department
Washington University

Objectives for the Sixth Budget Year

The main goal of this subcontract is to study the fluid dynamics of slurry bubble columns and address issues related to scaleup and design. The objectives set for the sixth budget year (October 1, 2000, – September 30, 2001) are listed below.

- Extension of the CARPT database to high superficial gas velocity in bubble columns.
- Extension of the CARPT/CT database to gas-liquid-solid systems at high superficial gas velocity.
- Evaluation of the effect of sparger design on fluid dynamics in bubble columns using the CARPT technique.
- Interpretation of LaPorte tracer data.
- Further improvement in Computational Fluid Dynamics (CFD) using CFDLIB and Fluent.

In this report, the research progress and achievements accomplished in the twenty-third quarter (October 1 – December 31, 2000) are summarized.

Highlights for the Twenty-Third Quarter

Implementation of Automated Calibration Device

- High-pressure CARPT calibration device has been designed and constructed.
- Successful testing has been performed at high pressure.
- Stepper motors have been added to the calibration device to provide the most accurate positioning of the tracer particle.
- A C++ program has been developed to control the movement of the calibration device and has been incorporated in the principal calibration program.

Evaluation of Tracer Position Reconstruction Strategies in the High-Pressure Bubble Column Reactor (HPBCR)

- A new robust and accurate tracer reconstruction approach has been developed based on a better understanding and modeling of the physics behind the photon emission phenomenon.

A New Data Acquisition Strategy

- A new tracer data acquisition strategy has been implemented that contains the spread in the calibration curve in a stainless steel column. This new data acquisition strategy enables the usage of the existing spline-based reconstruction method to provide reasonable estimates of the tracer location in a stainless steel column.

1. IMPLEMENTATION OF AUTOMATED CALIBRATION DEVICE

To determine the liquid and slurry velocity measurements at high pressure by the Computer Automated Radioactive Particle Tracking (CARPT) technique, all the detectors first must be calibrated at the operating conditions of interest. This calibration is accomplished by positioning the radioactive source and recording the radioactivity readings at all the detectors.

The high-pressure slurry bubble column reactor is made of stainless steel. The earlier method of calibration, which relied on fishing lines and hooks to position the radioactive particle, does not work because the column is not transparent and the system must be kept closed to maintain the high pressure. Hence, a different calibration device has been designed, constructed and successfully tested to accomplish the calibration in-situ at high pressure.

1.1 Design and Fabrication of the Device

The setup for the high-pressure bubble column is designed to handle a high airflow rate at a pressure of 200 psig. The stainless steel column of 6.3-in. diameter has a wall thickness of 3 mm. This thickness has been optimized to reduce the activity of the radioactive tracer particle. In addition, to avoid the radioactive beam attenuation due to wall thickness variation, the column is equipped with a minimum number of ports for pressure gauges, for liquid drainage and for checking overflow level via a small window. This column has been designed only for CAPRT/CT experiments. Another identical column for flow visualization and more intrusive probing of the flow patterns has already been designed and constructed and is equipped with several ports and transparent windows along the column. Figure 1.1 shows the CARPT setup with the stainless steel column. The detectors around the column have been accurately fixed at known positions with a Laser pointer.

The calibration with fishing lines and hooks is impossible in this opaque system, particularly in the high-pressure bubble column. The first version of the new calibration device was designed and constructed in CREL, as shown in Figure 1.2. This device is mounted at the top-flange of the column with a paper gasket and eight screws. It is equipped with a hand wheel for adjusting the axial level of the tracer particle via the vertical ruler and with a horizontal bar for controlling the angular motion of the tracer particle by 5^o increments. The device is equipped with hydraulic seals that can sustain pressures up to 1000 psig, as shown in Figure 1.3.

The detailed configuration of this calibration device is presented in Figure 1.2, which shows the external parts of the device, and in Figure 1.3, which illustrates the internal parts. The device consists of the following parts:

1. **Spider Support:** The spider-like support that carries the rod on which the radioactive tracer is mounted is made of three 3/8-in. diameter tubes (referred to as part number 1 in Figure 1.3). A ball is fixed at the end of each of the three tubes. The balls rotate in any direction to ensure that the support can move up and down and also rotate in the azimuthal direction. Attached to the balls are springs, which are under tension, always pushing the support-structure tubes against the column wall, so that the whole device is

supported rigidly. The springs also provide for a smooth azimuthal movement. The balls are of the same size and the springs have the same tension. The whole structure is fixed to two rigid ¾-in. diameter suspension rods (part 2 in Figure 1.3) with a length of about 14 in. These two rigid rods ensure that the whole device moves vertically without any bending and rotates without distortion. The particle-holding rod (part 3) has two sections. The upper section is made of stainless steel material, which is firmly fixed at the particle-holding base (part 4) with a screw. The lower section, where the radioactive tracer is fixed, is made of aluminum to reduce γ ray attenuation. The whole support and the particle-holding rod are designed to prevent the rod from vibrating when there is a turbulent flow in the column.

2. **Base for holding particle:** The base (part 4) is welded at the center below the spider. Special care has been taken to ensure perfect horizontality of the particle-holding base arm. This arm is absolutely perpendicular to the column wall. The arm of the particle-base has a number of specially machined guides for insertion of the particle-holding rod. Precise machining ensures that the particle-holding rod can be mounted at seven different radial locations, all parallel to the column wall.
3. **Suspension rods:** The suspension rods (part # 2 in Figure 1.3) are made of six pairs of stainless steel tubing of ¾-in. diameter and 14-in. length (which are connected with screws). This allows the extension of the structure to reach the bottom of the column. The suspension rods are made in six pieces because of the limited headspace at the top of the column. Scales for axial and angular divisions are engraved on the calibration device.
4. **Hydraulic seals:** The hydraulic seals of the suspension rods are tight enough to prevent the system from dripping when other suspension rods are introduced. This eliminates the need for locking the rods while adding to the structure.

The calibration device has been fabricated for the 6.3-in. diameter column to be used at atmospheric or elevated pressure. This device can be readily used for different column diameters with minor modifications.

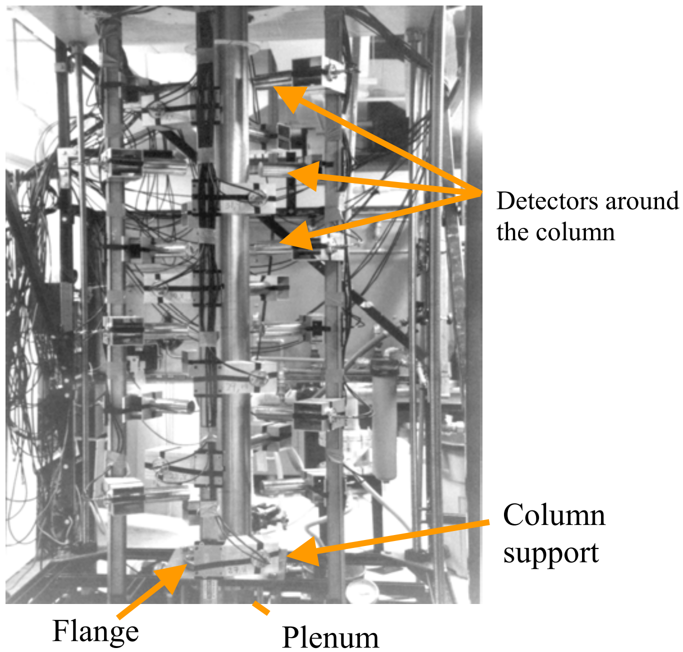

Figure 1.1 CARPT Setup for the High-Pressure Bubble Column

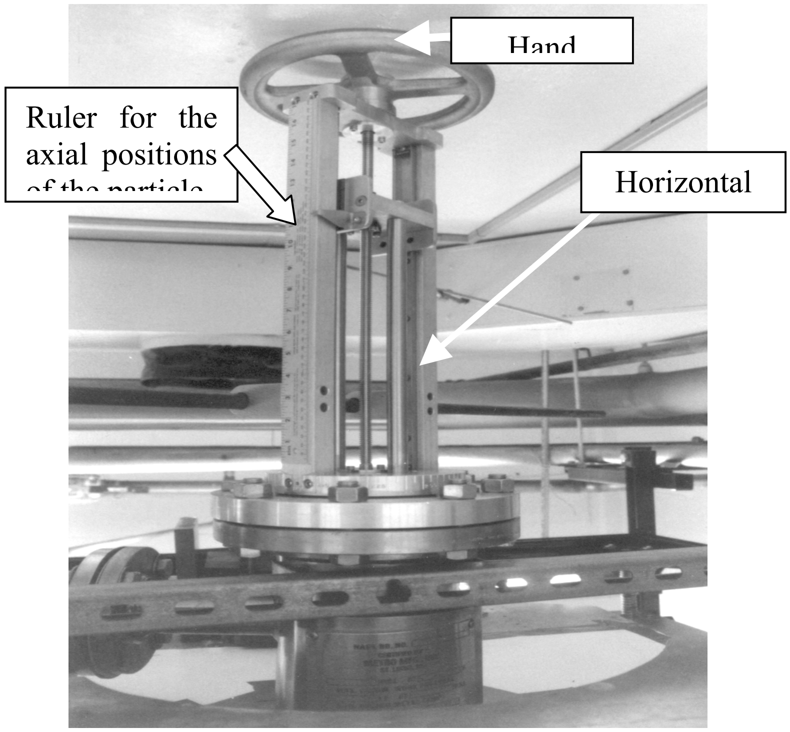

Figure 1.2 Calibration Device Mounted at the Top Flange of the Stainless Steel Column

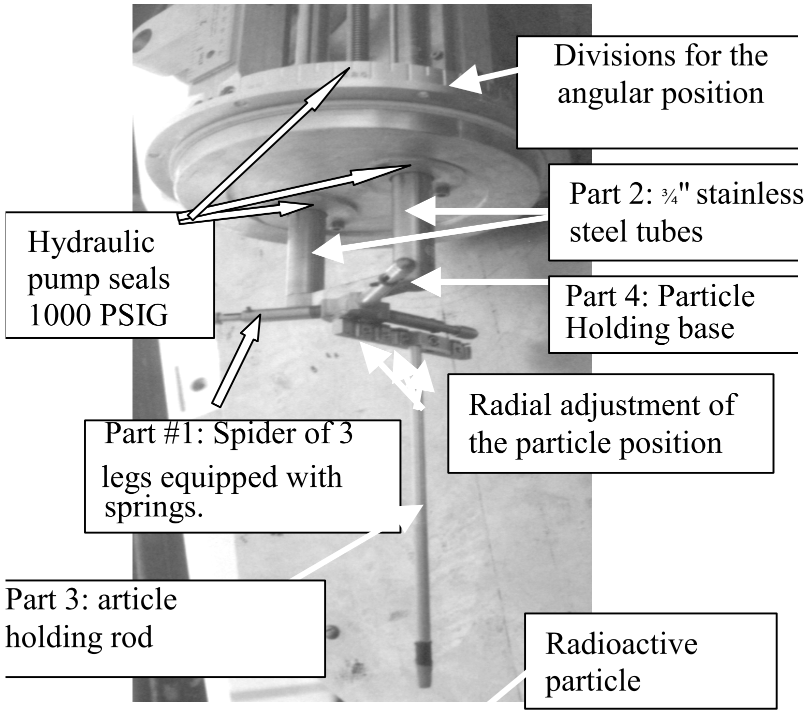

Figure 1.3 Parts Constituting the Calibration Device

1.2 Device Testing

The above-described calibration device has been used to perform the test calibration by acquiring signals from 2000 points in the column at a pressure of 3 atmospheres. The results were encouraging as no leak was observed, but considerable effort was required to move the particle in the azimuthal and axial directions. About 2 days were needed to perform this calibration. The calibration curves look similar to the ones obtained in bubble columns with the old calibration method (for example, Figure 1.4).

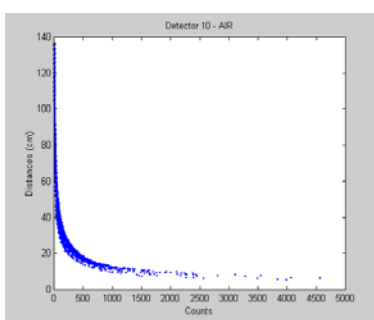

Figure 1.4 Calibration Curve Counts *vs* Distances for Detector 10

The calibration device was also tested at 7 atmospheres, and no leak was observed. To improve the ease of calibration at elevated pressures, stepper motors were added to the calibration device. This addition makes the calibration more accurate and eliminates the need to move the device manually. Figure 1.5 shows the modified final version of the calibration device when the stepper motors are added, one powerful motor for the angular movement (shown in Figure 1.5 by the large size motor) and another motor replacing the hand wheel for the axial movement. A sophisticated program has been developed in C++ to control the angular and axial movement of the calibration device. This program has been carefully inserted in the principal calibration program as a subroutine. It should be pointed out that the radial position of the tracer must still be changed manually by fixing the tracer support rod at different radial positions. The performance of this automated calibration device is excellent; about 4000 calibration data points were acquired in the stainless steel column within a record time of 8 to 10 hours. The path is now paved for CARPT experiments at elevated pressure.

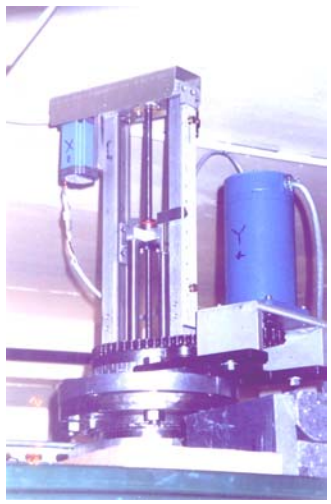

Figure 1.5 Automatic Calibration Device

2. EVALUATION OF TRACER POSITION RECONSTRUCTION STRATEGIES IN THE HIGH-PRESSURE BUBBLE COLUMN REACTOR (HPBCR)

2.1 Problem Definition

The first step in a CARPT experiment is to obtain a calibration map of the count registered by each detector for several hundred known locations of the tracer. A typical calibration curve obtained in a Plexiglas column is shown in Figure 2.1.

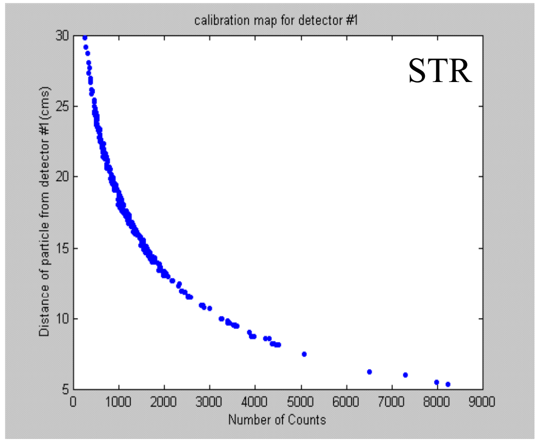

Figure 2.1 Calibration Map Obtained in a Plexiglas Stirred Tank Reactor

From Figure 2.1 it is clear that each count registered by a detector is associated with a unique distance of the tracer from that detector. For instance if detector #1 registers 3000 counts, then the tracer particle is 10.0 cm from detector #1. Hence this calibration curve can be expected to provide an accurate reconstruction of the distance of the tracer from each detector, which can then be used to obtain the exact tracer co-ordinates by solving a system of linear equations (Devanathan, 1991). However, when calibration experiments were performed in air in the stainless steel column, the calibration curve obtained looked very different, as shown in Figure 2.2.

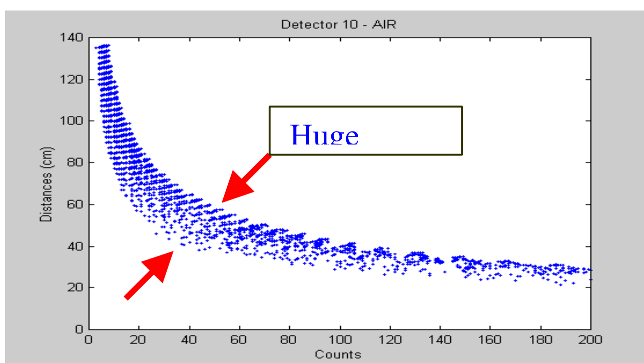

Figure 2.2 Calibration Map Obtained in the Stainless Steel Reactor

The calibration curve obtained in the stainless steel column shows a huge spread. With a curve of this form, the conventional approach of generating a spline of the form

$$d_{10} = f_{10}(C_{10}) - \quad - \quad -(2.1)$$

where d_{10} is the tracer distance from detector 10 and C_{10} is the count recorded at detector 10, will not work well, because if we feed a count of 100 (C_{10}) to equation (2.1), then the predicted distance d_{10} is 36 cm, while Figure 2.2 suggests that the distance of the tracer from detector 10, d_{10}, can be anywhere between 30-42 cm. This clearly indicates that the spline-based approach to fitting the count vs the distance data of Figure 2.2 would result in a considerable error in estimating the distances accurately. Further, it has been observed that even small errors in the reconstructed distances (~1-2mm) can be amplified considerably when solving for the exact tracer co-ordinates using the weighted least-squares regression technique (Devanathan, 1991). Hence, for systems in which the calibration curve looks like that shown in Figure 2.2, the existing approach cannot be used to reconstruct even the known calibration points, as illustrated clearly by Figure 2.3.

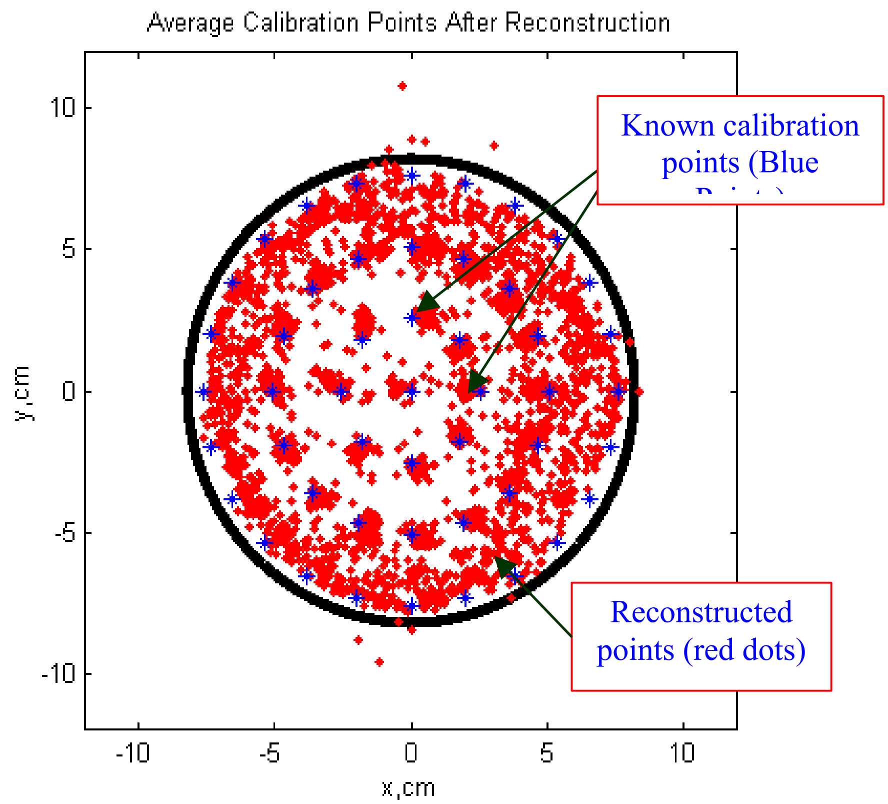

Figure 2.3 Reconstruction of 3528 Known Calibration Points

Figure 2.3 is a comparison between the actual calibration points shown by the blue points (3528 in all, corresponding to 49 points per axial plane and around 72 axial planes) and the reconstructed points (the red dots). Ideally the red dots should have fallen directly on top of the blue dots (implying exact reconstruction of calibration points). The spread of the red dots around each blue dot corresponds to the reconstructed location at each axial plane. This clearly illustrates that the existing spline-based reconstruction approach cannot be used to reconstruct even the known calibration points. As expected, the errors in reconstructing other tracer locations are larger, as shown in Figure 2.4.

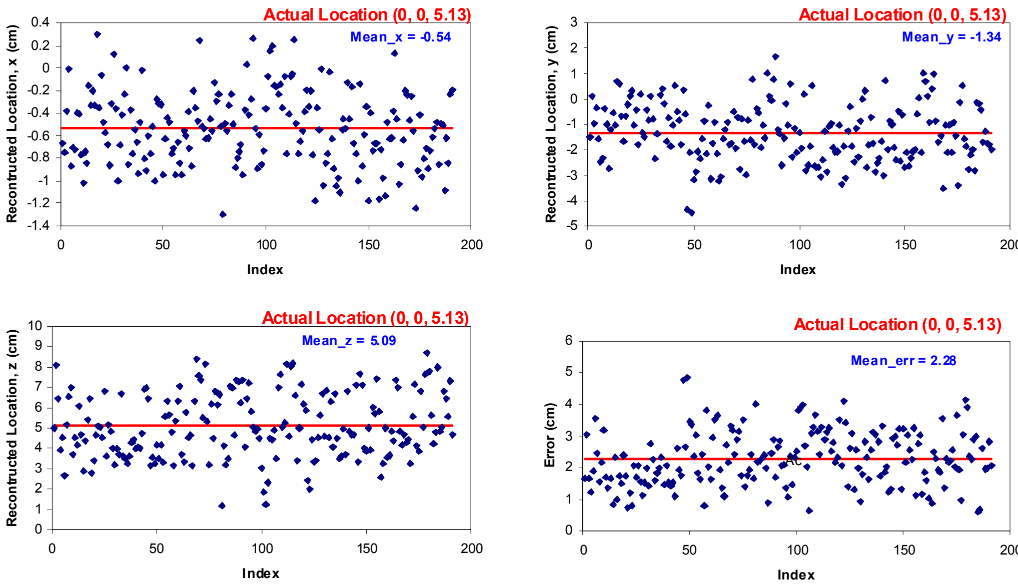

Figure 2.4 Reconstruction of Unknown Test Points Located at
(r = 0 cm, θ = 0°, z = 5.13 cm)

Hence, the problem was identified to be the use of the existing spline-based reconstruction approach for systems whose calibration curve looks like that shown in Figure 2.2, and the further amplification of this error by use of the existing weighted least squares regression technique in identifying the exact tracer co-ordinates (x,y,z).

To remedy this situation, a two-pronged approach has been adopted in which i) the spline-based reconstruction and the weighted least squares regression are replaced by different approaches and ii) a new data acquisition strategy is outlined that confines the spread in the calibration curve, thus allowing the use of the existing reconstruction algorithms. Both are expected to provide better reconstruction of the calibration, as well as the unknown test points. The two new tracer position reconstruction approaches are outlined below, and in a separate follow-up section the new data acquisition protocol is discussed and illustrated.

2.2 New Reconstruction Approaches

2.2.1 A Look-Up Table Approach

Larachi et. al. (1994) used a two-step approach to reconstruct the unknown tracer position. In the first step they used the calibration data spread on a coarse grid (using only a few hundred calibration data) to generate the system constants such as detector dead times (τ_d), detector gains (R) and attenuation coefficients of the medium (μ_l, μ_g, etc.). They used these constants in a model that then generated an estimate of the counts for any particular position of the tracer with respect to a selected detector given by

$$C_{est} = \frac{T\nu R\phi\varepsilon}{1+\tau\nu R\phi\varepsilon} - - -(2.2)$$

where T is the sampling period (sec), ν is the number of γ ray photons emitted per disintegration of Sc^{46} ($\nu = 2$), ϕ is the photopeak efficiency and ε is the total intrinsic detection efficiency of the detector. The notations used are exactly the same as in Larachi et. al. (1994). This model was then used to generate a finer grid of calibration data that was then stored in the form of a lookup table. This is schematically outlined in Figure 2.5.

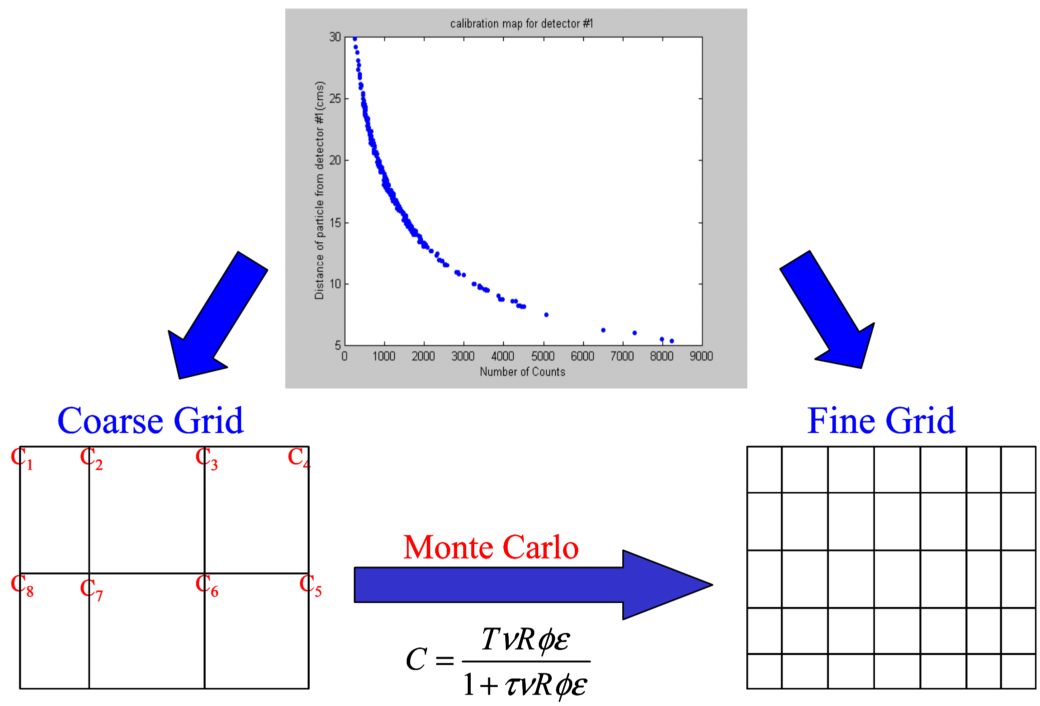

Figure 2.5 Generation of a Fine Grid of Calibration Data Either by Monte Carlo Simulations or Through Experiments

This first step of the Larachi et. al. (1994) procedure is redundant when calibration experiments have been performed on a dense grid as in the stainless steel reactor (3,528 points). Hence the calibration data can be organized directly into a lookup table, as shown in Figure 2.6.

X	Y	Z	C_1	C_2	C_3	C_4	C_5	C_6	C_7	C_8	C_9	C_{10}	C_{11}	C_{12}	C_{13}	C_{14}	C_{15}	C_{16}
0	0	0	396	420	12	37	45	89	120	5	56	71	80	110	92	370	41	4
0	0.2	0	--	---	---	---	---	---	---									
..	..																	..

Figure 2.6 Calibration Information Organized as a Lookup Table

The lookup table stores the co-ordinates of each calibration point and the corresponding time-averaged count registered by each detector. To reconstruct an unknown tracer location, a quantity called the chi squared (χ^2) is computed at each node. The χ^2 is defined as follows:

$$\chi^2(j) = \sum_{i=1}^{N_D=16} \frac{(C_i - M_i)^2}{\sigma_i^2} \qquad (2.3)$$

where j is the j^{th} calibration node, C_i is the count registered by the i^{th} detector at the j^{th} node (obtained from the lookup table), M_i is the count measured by the i^{th} detector when the particle is kept at an unknown location and $\sigma_i^2=C_i$. This χ^2 is computed for all the known calibration points (i.e., j=1 to 3528). The node that minimizes the χ^2 is identified as the node closest to the unknown point. The time-averaged counts corresponding to the known calibration points in the HPBCR are then fed into this algorithm. The algorithm yields perfect reconstruction of the calibration points, as shown in Figure 2.7.

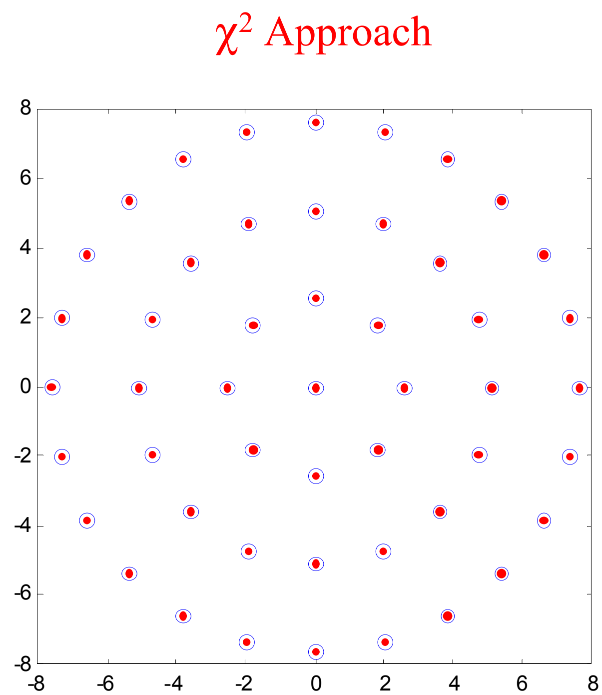

Figure 2.7 Reconstruction of 3,528 Known Calibration Points

This new algorithm, which does not use the spline-fitting/weighted least regression technique, clearly does an excellent job of reconstructing the known calibration points. Now the performance of this algorithm in reconstructing the unknown tracer location has to be evaluated. With the new algorithm, exact reconstruction is possible (as seen from Figure 2.7), provided the unknown point lies on the calibration nodes. However, if the unknown point lies in between the nodes, then the algorithm in its existing form cannot be expected to do a good job of reconstructing the unknown tracer location unless the calibration grid is extremely fine (Δx, Δy, Δz~0.05-0.1 mm). Hence, a second iteration has to be performed to identify the exact location of the unknown point. This is done by following the ideas outlined in Larachi et. al. (1994). They generate a fine grid around the closest node identified in the first iteration, as shown in Figure 2.8.

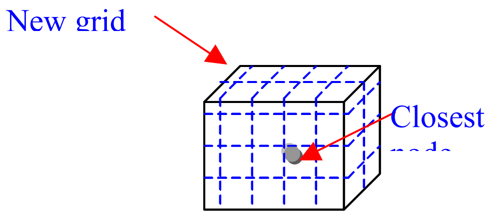

Figure 2.8 Generation of a Fine Mesh Around Closest Node

The new grid can be generated by an approximate formula given below:

Count at new node

Sampling Time

Detector dead-time

$$C = \frac{TC_{ref}\left(\frac{r_{ref}}{r}\right)^2 \exp\left(\mu_R\left(\delta_{ref}-\delta\right)\right)}{T-\tau C_{ref}+\tau\left(\frac{r_{ref}}{r}\right)^2 C_{ref}\exp\left(\mu_R\left(\delta_{ref}-\delta\right)\right)} \quad \text{- - -} \quad (2.4)$$

Distance traveled by photon before striking detector

Tsoulfanidis (1983)

Count at closest node

The information corresponding to the new grid is organized as a lookup table similar to Figure 2.6. The same criterion of χ^2 is then used to identify the exact location of the unknown test location. The formula in Equation (2.4) permits evaluation of the contribution of different physical phenomena like the effect of detector response time (τ_d), attenuation coefficient of the medium and attenuation coefficient of the stainless steel wall (μ_R). Three different approximations of (2.4) were used to evaluate the contribution of the different physical phenomena. The first model (M_1) ignored the attenuation coefficients and the detector dead times (i.e., μ_R and τ_d were set to zero), the second model (M_2) ignored the attenuation coefficient of the medium and the third model was the full model (M_3). The ability of M_1 and M_3 to reconstruct ten unknown test points is presented in Table 2.1.

Model	**M_1**	**M_3**	**M_1**	**M_3**
S.N.	**σ_r (cm)**	**σ_r (cm)**	**σ_z (cm)**	**σ_z (cm)**
1	0.64	0.55	0.31	0.20
2	0.78	0.67	0.20	0.06
3	0.74	0.77	0.40	0.31
4	0.72	0.66	0.21	0.09
5	0.56	0.61	0.16	0.11
6	0.57	0.69	0.18	0.06
7	0.60	0.59	0.26	0.12
8	0.66	0.59	0.18	0.18
9	0.77	0.60	0.25	0.20
10	0.57	0.61	0.18	0.18

Table 2.1 Reconstruction Accuracy of Ten Test Points using Model M_1 and M_3

From Table 2.1 it is clear that the model that accounts for the attenuation coefficient of the column wall is more accurate than model M_1, which ignores μ_R. The comparisons also suggest that while there are clear improvements in the accuracy of the axial co-ordinate reconstruction, not much improvement is seen in the reconstruction of the radial co-ordinate. The poorer resolution in the radial co-ordinate has little to do with the stainless steel column wall, and instead may be due to the presence of only two detectors at each axial plane (Roy et. al., 1999). The radial co-ordinate reconstruction worsened when only one detector per axial plane was used for the reconstruction, which confirms this assertion. Calculations also revealed that attenuation caused by the presence of the stainless steel column wall was sometimes as high as that encountered by a photon beam traveling ten times the distance in water (i.e., $\delta_{ss}=10\delta_{water}$). A comparison of the errors using M_3 in reconstruction indicates that the mean errors are much lower than the mean errors seen in Figure 2.4. Thus, it can be concluded that the new approach yields a definite improvement in reconstruction of the calibration points, as well as the unknown tracer locations.

2.2.2 Full Monte Carlo Approach

The comparisons between the three different models M_1, M_2 and M_3 suggested that modeling the "physics" of the different phenomena may improve the reconstruction accuracy. Hence, a full Monte Carlo model was developed in which the first step is similar to Larachi et. al. (1994), i.e., a Monte Carlo simulation is done to obtain calibration data on a finer grid (refer to Figure 2.9). However, a full Monte Carlo simulation with the HPBCR calibration data revealed that counts predicted by Monte Carlo simulations are often higher than the measured counts, as shown below in Figure 2.9. The overall percentage deviation with respect to the 45^o parity line was found to be positive, indicating that Monte Carlo overestimates the actual counts.

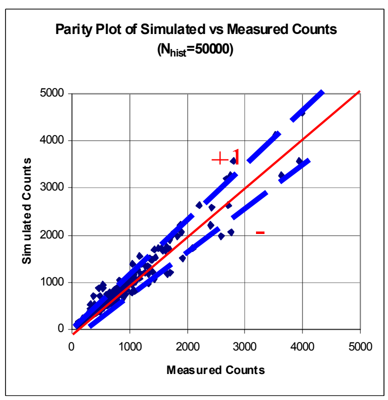

Figure 2.9 Comparison between Measured and Simulated Counts

This indicates that the presence of the "stainless steel" wall is causing the phenomenon of buildup to occur (Tsoulfanidis, 1983). Equation (2.2), used to generate a Monte Carlo estimate of the count, does not account for the phenomenon of buildup, which might explain the observed over-prediction in counts. Hence, a Monte Carlo simulation done with data containing the full energy spectrum will need to account for the phenomenon of buildup, which is not a trivial matter. The presence of buildup was confirmed by comparing the spectrum measured with and without stainless steel wall (Figures 2.10a and 2.10b).

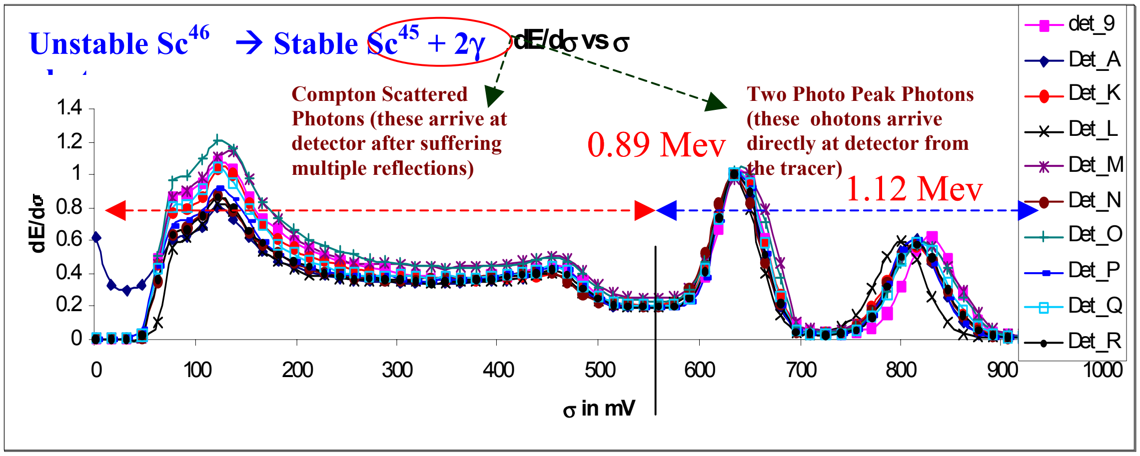

Figure 2.10a Photo Energy Spectrum Obtained in a Plexiglas Column

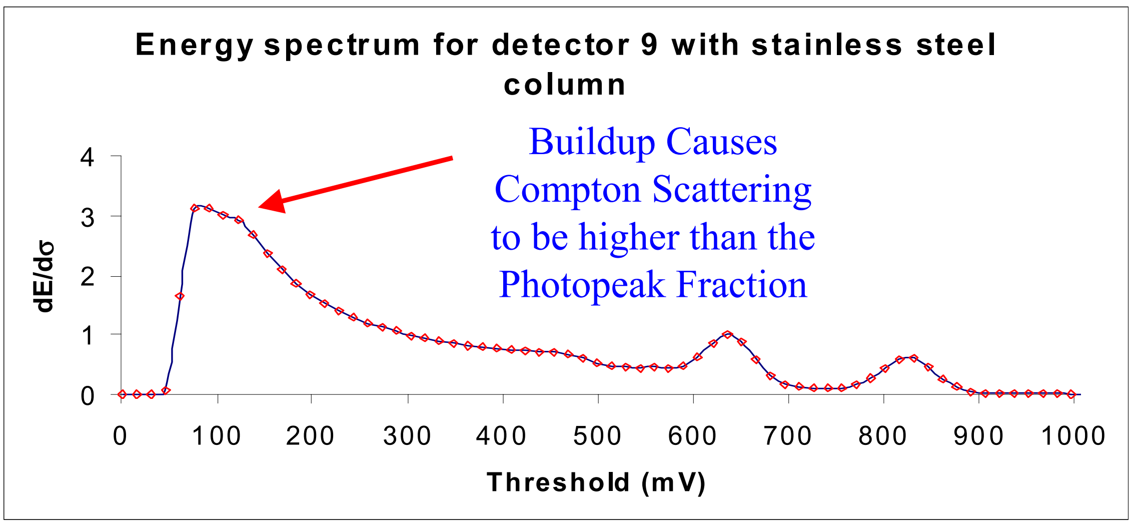

Figure 2.10b Photo Energy Spectrum Obtained in a Stainless Steel Reactor

Some preliminary attempts were made to model the phenomenon of buildup by developing an iterative neural network-based algorithm. The iterative scheme was not robust and did not yield converged results for the buildup function. Hence this approach was not further pursued. The only way to avoid modeling buildup is to constrain the detectors to acquire only the photopeak fraction of the photon energy spectrum. This means that the detectors should be constrained to collect only those photons with energy greater than 600mv (see Figures 2.10a and 21.0b). Then one can be certain that the data will not be corrupted by the buildup phenomenon. Some preliminary Monte Carlo simulations were done by acquiring data with a threshold of 560mV to register only the photopeak fraction. Monte Carlo simulations were carried out with 1000 photon histories. A fine grid of calibration data was generated using Monte Carlo simulations. The parity plots of the simulated vs measured counts for the new data set are shown in Figure 2.11, which reveals improvement compared to Figure 2.9.

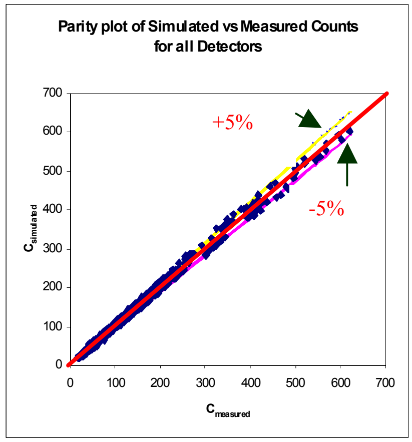

Figure 2.11 Comparison Between Measured and Simulated Counts

The parity plots indicate that simulated counts compare well with the measured counts. Thus in Sections 2.2.1 and 2.2.2, two new reconstruction approaches have been outlined, both of which are based on modeling the physics of the photon emission phenomenon. Both of these approaches seem to give a reasonably good reconstruction of the tracer location. The second approach (Section 2.2.2) also suggests that the phenomenon of buildup due to the presence of stainless steel column walls might be the cause for the large spread in the calibration curve (refer to Figure 2.2). This suggestion led us to explore a new data acquisition strategy, as outlined below.

3. A NEW DATA ACQUISITION STRATEGY

This strategy is based on the assumption that the observed scatter in the calibration curve is caused by buildup at the stainless steel column wall. Through Figures 2.10a and 2.10b, we also established that the presence of buildup affects only the Compton scattering portion of the energy spectrum and not the photopeak fraction of the spectrum. Hence the new data acquisition strategy was to acquire only the photopeak fraction of the energy spectrum and then examine the appearance of the calibration curve. These calibration experiments were performed in a stainless steel column (O.D.= 10.4 in (26.4 cm) and thickness = 0.24 in (0.6 cm)) surrounding an 8.5 in (21.6 cm) stirred tank reactor with the impeller rotating at 400 rpm (corresponding to tip speed of V_{tip}=1.4 m/s), with gas being sparged at 10.0 scfh. The resulting calibration curve is shown in Figure 3.1:

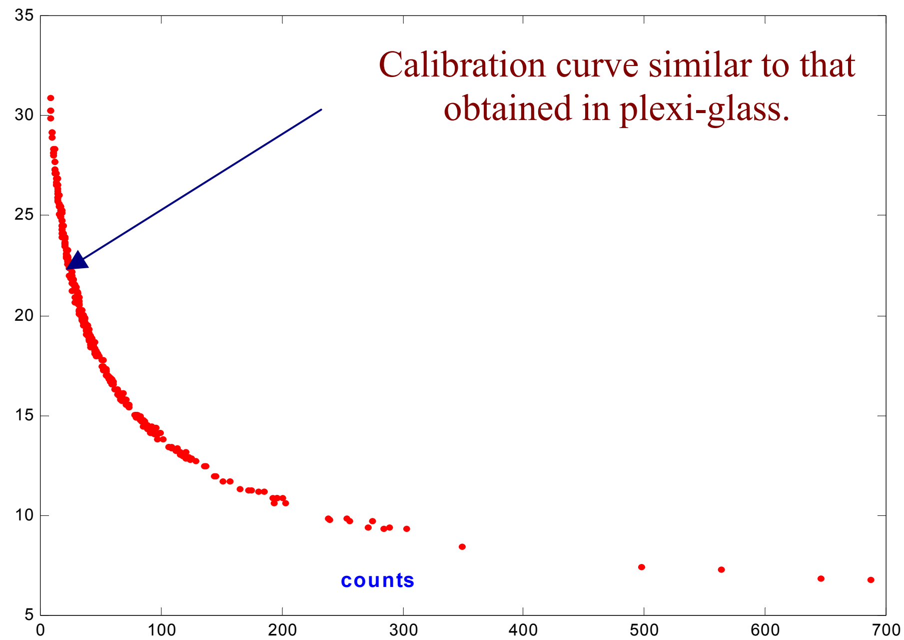

Figure 3.1 Calibration Curve Obtained in S.S. Column for Detector #1 by Acquiring Photopeak Fraction Alone

Figure 3.1 suggests that acquiring only the photopeak fraction of the energy spectrum results in a calibration curve that is very similar to the calibration curve obtained in the Plexiglas column (refer to Figure 2.1), with the only difference being the gradient of the calibration curve in the range of tracer to detector distances that are of interest. The gradient of the calibration curve depends on the attenuation coefficient of the intervening medium. In a stainless steel column, the gradient of the calibration curve is steeper than in a Plexiglas column due to the higher attenuation coefficient of the stainless steel column wall. The above calibration curve suggests that with this new data acquisition strategy, particle reconstruction should be reasonably accurate with the existing spline/weighted least squares regression approach. Hence, the time-averaged counts registered by each detector corresponding to the known calibration points were fed to the existing spline-based reconstruction approach. The details of reconstructing the 396 known calibration points are shown in Figures 3.2a and 3.2b. These figures suggest that the existing spline-based approach can reconstruct the known calibration points well, except for the calibration points near the bottom, top and walls of the column. The reconstruction is definitely much better than seen earlier (Figure 2.3).

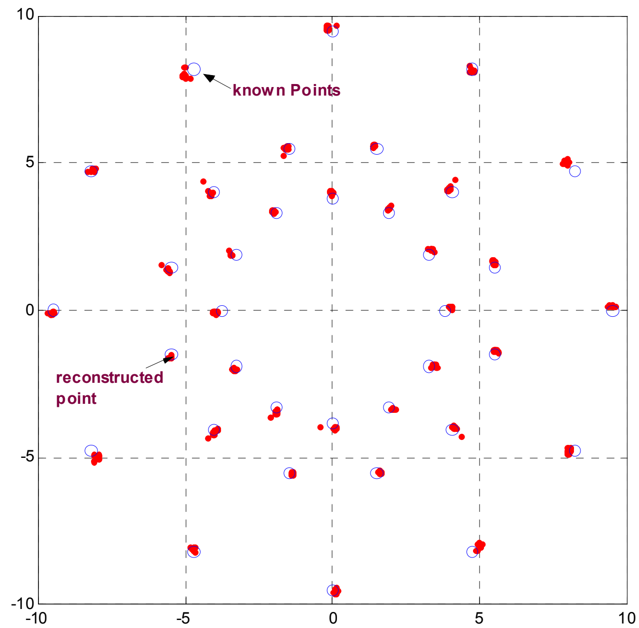

Figure 3.2a Reconstruction of 396 Known Calibration Points Projected onto a Horizontal Plane

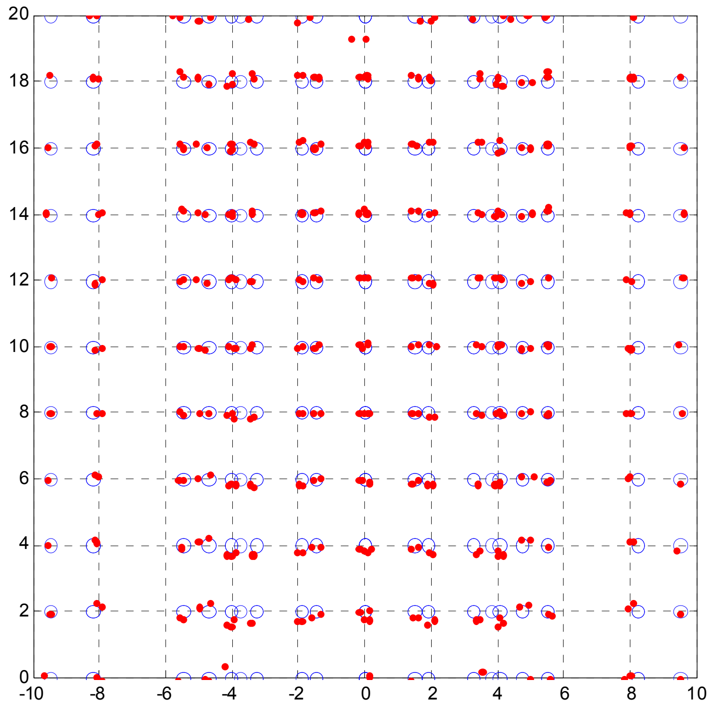

Figure 3.2b Reconstruction of 396 Known Calibration Points Projected onto an r-z Plane

In both Figures 3.2a and 3.2b the blue circles represent the known calibration points, while the red dots represent the reconstructed point. Further, the spline-based approach was used for reconstructing 36 test locations (corresponding to 3 radial locations 3.8, 5.7 and 9.5 cm, θ=0-360^o, z=0-20 cm, $\Delta\theta$=30^o and Δz=2.0 cm). The details of reconstructing a set of 12 test points corresponding to one axial plane (z=5.0 cm) are shown in Figure 3.3. The figure suggests that, corresponding to the 256 instantaneous samples acquired for each test point is a distribution in the reconstructed co-ordinate at that point. This distribution around each test point is not circular, but elliptical. However, the major axis of the ellipse is oriented in the same angular direction as the test point. The mean radial location of each distribution is 7.02 cm, suggesting that there is a negative bias in the reconstructed radial mean locations (i.e., underestimate in radial location). Since there is a bias in the estimated mean radial location, when variances are computed with respect to the real radial location (i.e., 7.2 cm) these do not converge with an increase in the number of samples. Hence the variances were computed around the reconstructed radial location. This σ_r is of the order of 4.0 mm, which is comparable to σ_r reported by Larachi et. al. (1994), that is, a radial σ_r of 2.5-3.0 mm when they acquired data at 33 Hz.

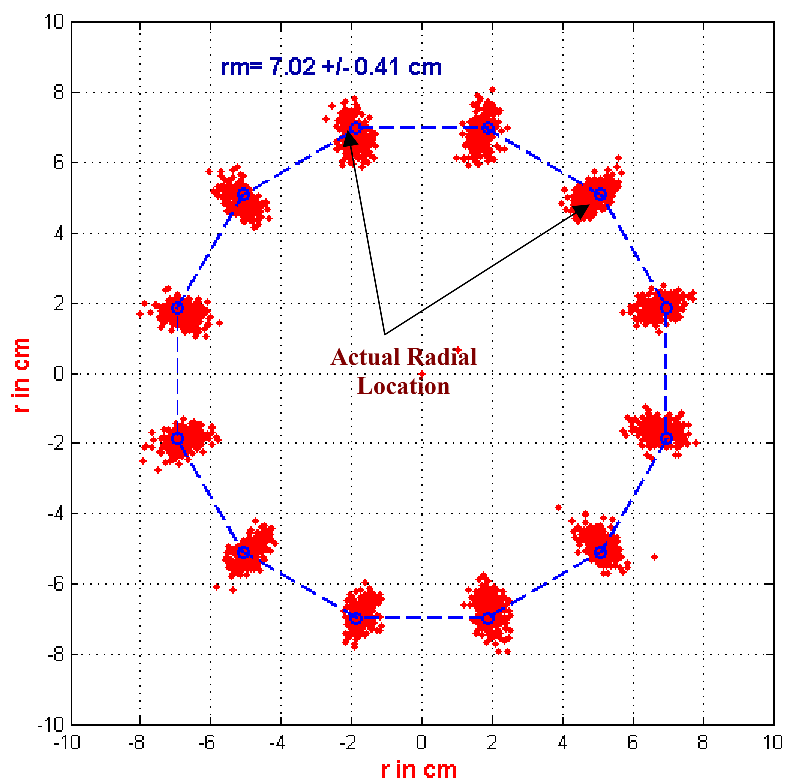

Figure 3.3 Details of Reconstructing 12 Test Points (r=7.2 cm, θ=15^o-345^o, z=5.0cm) from 3072 Instantaneous Samples Acquired at 50 Hz

They have also shown that the radial variance and the axial variance decrease with a decrease in sampling frequency and increase with an increase in sampling frequency. This variation from Larachi et. al.'s work (1994) is reproduced in Figure 3.4.

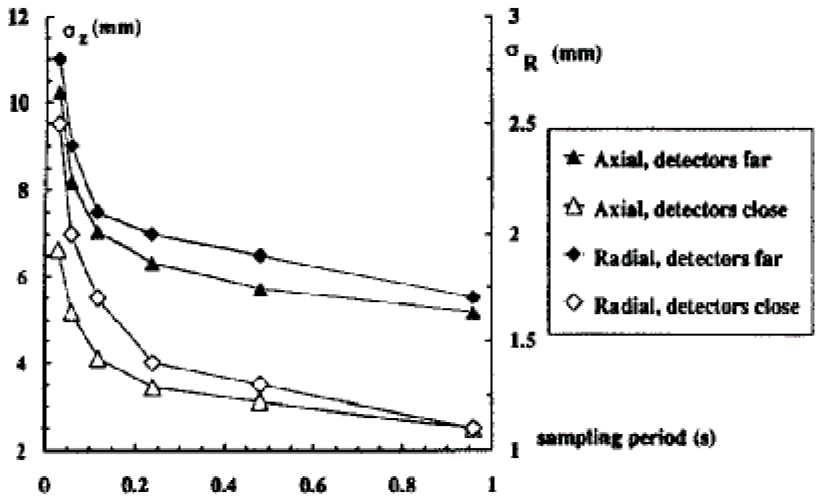

Figure 3.4 Variation in σ_r and σ_z with Sampling Frequency

However, it must be noted that while the variation in Figure 3.4 was obtained with 8 detectors, the current study used 16 detectors. Also Larachi et. al.'s (1994) experiments were conducted in a Plexiglas column with a tracer of strength 200μCi, while the current experiments were carried out in a stainless steel column with a tracer of strength 200μCi. Furthermore, Larachi et. al.'s column diameter was 4 inches, while the current setup diameter is 10.4 inches. Given all these differences, the radial σ_r obtained in the current study seems reasonable. The accuracy in reconstructing all the 36 test locations is summarized in Table 3.1.

Location	**R_{actual} (cm)**	**R_{recon} +/- σ_r (cm)**	**Z_{actual} (cm)**	**Z_{recon} +/- σ_z (cm)**
1	**7.2**	**7.02 +/- 0.41**	**5.0**	**5.1 +/- 0.45**
2	**7.2**	**6.93 +/- 0.38**	**10.0**	**10.0 +/- 0.40**
3	**7.2**	**6.96 +/- 0.40**	**15.0**	**14.9 +/- 0.46**

Table 3.1 Summary of Reconstruction Accuracy of 36 Test Locations (1 radial location, 3 axial locations and 12 angular locations)

Table 3.1 suggests that the estimate of the mean radial location as well as the mean axial location is biased. The radial estimate is always negatively biased, while the axial estimate is positively biased in the center of the column, but towards the top it is negatively biased. The σ_r and σ_z are all comparable and are between 4.0-4.5 mm. These numbers are comparable to similar values reported by Larachi et. al. (1994). On the face of it, the σ_z (4.0-4.5 mm) from the current study may seem to be better than those of Larachi et. al. (9.5 –11.0 mm). However, it must be kept in mind that Larachi et. al.'s study used only 8 detectors, while in the current study 16 detectors were used. In order to analyze the effect of detector configuration and number of detectors, the above analysis was repeated for two different detector configurations. In the first detector configuration only 8 detectors were used, as shown in Figure 3.5:

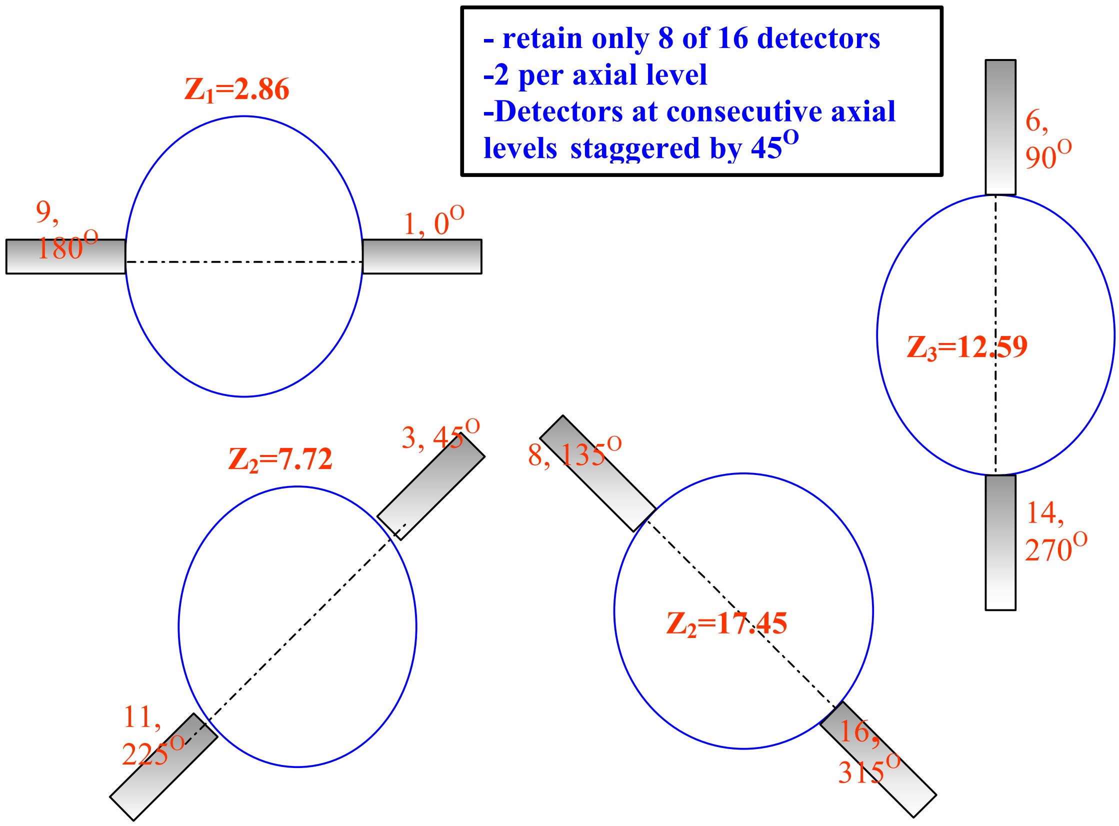

Figure3.5 Analysis of Effect of Detector Configuration on Reconstruction Accuracy

The accuracy in reconstructing the 36 test points after hiding 8 detectors is reported in Table 3.2.

Location	R_{actual} (cm)	R_{recon} +/- σ_r (cm)	Z_{actual} (cm)	Z_{recon} +/- σ_z (cm)
1	7.2	7.08 +/- 0.69	5.0	5.31 +/- 1.29
2	7.2	7.05 +/- 0.65	10.0	9.92 +/- 1.11
3	7.2	7.00 +/- 0.73	15.0	14.22 +/- 1.44

Table 3.2 Summary of Reconstruction Accuracy of 36 Test Locations (1 radial location, 3 axial locations and 12 angular locations) after not including 8 Locations

Table 3.2 suggests that by not including 8 detectors in the analysis, the error in the estimate of the mean axial location has increased. The σ_r and σ_z have also increased, with $\sigma_r(8)/\sigma_r(16) \sim 1.75$ and $\sigma_z(8)/\sigma_z(16) \sim 3.0$. The σ_z appears large (11-14 mms), but is comparable to the values reported by Larachi et al. with 8 detectors. Hence Table 3.2 suggests that the number of detectors used for reconstruction definitely affects the reconstruction accuracy. This was also the case when only 4 detectors were used for reconstruction. These results are summarized in Figures 3.6a and 3.6b, respectively.

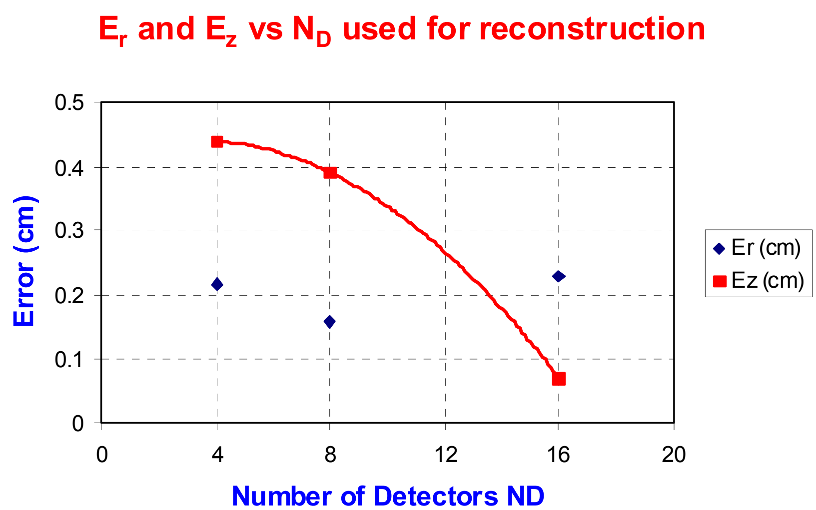

Figure 3.6a Variation of Radial and Axial Bias with Number of Detectors used for Reconstruction

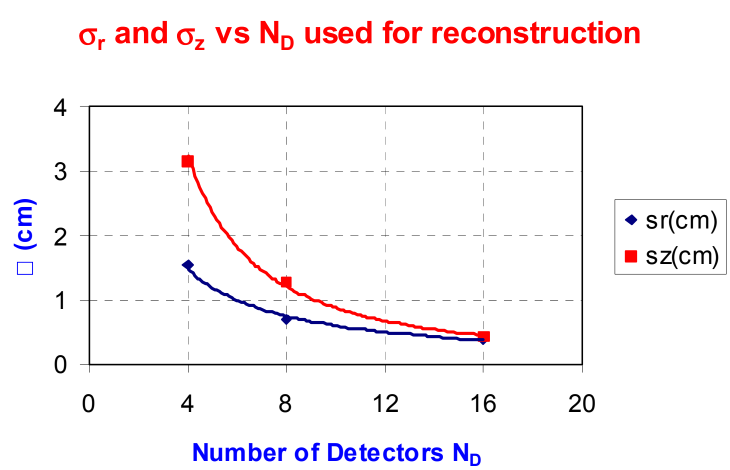

Figure 3.6b Variation of σ_r and σ_z with Number of Detectors used for Reconstruction

Figure 3.6a suggests that the bias in the radial estimate is little affected by the number of detectors used for reconstruction, while the bias in the axial estimate decreases with an increase in the number of detectors (4.0 to 0.5 mm). Figure 3.6b suggests that σ_z is comparable to σ_r for a large number of detectors, and σ_z and σ_r progressively increase as the number of detectors decreases. The rate at which σ_z increases is higher than the rate at which σ_r increases. This suggests that the error boundaries associated with the particle position reconstruction change from a sphere (when N is large) to an ellipsoid (when N is small). To generalize these results, one would need to look at the variation of σ_r and σ_z with detector density (defined as N_D/(Active volume of interest in reactor)). The above analysis suggests that with the new data acquisition strategy, even the existing spline-based/weighted regression technique can be used to obtain reasonably good estimates of the tracer location in the stainless steel column. Hence this approach will be used for the time being for analysis of CARPT experiments performed in the High Pressure Bubble Column reactor at the conditions of interest.

Future Work

Future work planned for Washington University includes the three-dimensional simulation of two-phase flows (air and water) in bubble columns, using CFDLIB.

References

Devanathan, N., Investigation of liquid hydrodynamics in bubble columns via computer automated radioactive particle tracking (CARPT), D.Sc., Saint Louis, Missouri (1991).

Larachi, F., G. Kenedy and J. Chaouki, A γ-ray detection system for 3-D particle tracking in multiphase reactors, *Nucl. Instr. and Meth.*, **A338**, pp.568-576 (1994).

Roy, S., F. Larachi,, M.P. Dudukovic', R. Dodson, and M.H. Al-Dahhan, Implementation of computer automated radioactive particle tracking (CARPT) on a gas-solid riser: experiment design and analysis, CREL Internal Report (1999).

Tsoulfanidis, N., Measurement and detection of radiation, McGraw Hill, New York (1983).